Because it is unlikely that the mantle transition zone is thicker (colder) than normal beneath all the geological regions in receiver function studies [(*7*–*9*); K. G. Dueker and A. F. Sheehan, *J. Geophys. Res.* **102**, 8313 (1997); A. Li, K. M. Fisher, M. E. Wysession, T. J. Clarke, *Eos Fall Suppl.* **78**, F11 (1997)], except for Iceland, we do not use the average from *SS* precursors as the reference transition zone thickness in this study. If the oceanic average from *SS* precursors is a more appropriate representation of the transition zone thickness beneath normal oceans, then the mantle transition zone beneath the SEPR is thicker and colder than normal, inconsistent with models of active thermal upwelling.

25. S. van der Lee, H. Paulssen, G. Nolet, *Phys. Earth Planet. Int.* **86**, 147 (1994).
26. D. K. Lee and S. P. Grand, *Geophys. Res. Lett.* **23**, 3369 (1996).
27. D. R. Toomey *et al.*, *Science* **280**, 1224 (1998).
28. C. J. Wolfe, *ibid.*, p. 1230.
29. C. R. Bina and G. Helffrich, *J. Geophys. Res.* **99**, 15853 (1994).
30. We thank the MELT Instrument Teams for their efforts. This research was supported by the U.S. National Science Foundation.

19 February 1998; accepted 17 April 1998

Phase Velocities of Rayleigh Waves in the MELT Experiment on the East Pacific Rise

Donald W. Forsyth,* Spahr C. Webb, LeRoy M. Dorman, Yang Shen

The phase velocities of Rayleigh waves increase more rapidly with distance from the East Pacific Rise (EPR) axis than is predicted by models of conductive cooling of the lithosphere. Low velocities near the axis are probably caused by partial melt at depths of 20 to 70 kilometers in a zone several hundred kilometers wide. The lowest velocities are offset to the west of the EPR. Wave propagation is anisotropic; the fast direction is approximately perpendicular to the ridge, parallel to the spreading direction. Anisotropy increases from a minimum near the axis to 3 percent or more on the flanks.

Rayleigh waves are elastic waves that travel along the surface of Earth. Although the phase velocity of the wave is weakly dependent on the density and compressional velocity of the medium, the primary sensitivity is to the shear wave velocity (*1*). The peak sensitivity of Rayleigh waves to shear velocity is at a depth of about one-third of a wavelength, or 30 to 35 km for a 25-s period wave, for example. The phase velocity at 25 s is an integrated measure of the shear velocity structure in the upper 100 km of the mantle; the strongest response is for depths of 20 to 70 km, which is expected to be the primary melt production zone (*2*, *3*).

Previous studies of Rayleigh and Love surface waves crossing the oceans from distant, teleseismic earthquakes recorded at island and continent stations indicate that phase velocities increase systematically with increasing age of the sea floor (Fig. 1), in agreement with thermal models for cooling of the oceanic lithosphere. The change in average velocity from the youngest sea floor, less than 4 or 5 million years old, to the average velocity in the next age zone, however, is two to three times larger than could be explained by conductive cooling of the mantle and is caused by a zone of anomalously low shear velocities centered at a depth of 40 to 60 km (*4*). Melt fractions of a few tenths to 5%, depending on the aspect ratio of the melt pockets, are sufficient to explain these anomalous velocities. In young sea floor with normal crustal thicknesses, any area with phase velocities less than about 3.85 km/s at a 25-s period probably is affected by the presence of partial melt. Global teleseismic studies, however, lack the resolution to determine the width of the zone of partial melting or the lowest velocities at the ridge axis. The Mantle Electromagnetic and Tomography (MELT) Experiment was designed to provide spatial resolution that is limited primarily by the physical averaging associated with finite wavelength waves, not by station or event geometry.

Some teleseismic studies have found that Rayleigh waves propagate faster perpendicular to the East Pacific Rise (EPR) (*5*, *6*). This azimuthal anisotropy is attributed to a pattern of flow in the mantle that aligns the *a* axis of olivine crystals perpendicular to the ridge axis. The conclusion that anisotropy is required has been controversial, because there are trade-offs between a simple pattern of anisotropy and a more complicated pattern of heterogeneous, isotropic velocities. In a weakly anisotropic medium, the phase velocity c is expected to be of the form $c(\omega, \psi) = A_0(\omega) + A_1(\omega)\cos 2\psi + A_2(\omega)\sin 2\psi + A_3(\omega)\cos 4\psi + A_4(\omega)\sin 4\psi$, where ω is the frequency, ψ is the azimuth of propagation of the wave, and A_0 and A_4 are velocity coefficients. Theoretical studies indicate that 4ψ variations should be small for Rayleigh waves (*7*), so we neglect them here.

We selected for analysis records (*8*) from 23 earthquakes distributed around the margins of the Pacific. An estimate of the variation of phase velocity with age in the MELT study area can be obtained from the records of a single event. The magnitude 7.3 event of 21 February 1996 off the coast of northern Peru lies within 1° of the extension of the great circle path along the primary array of ocean bottom seismometers (OBSs). Assuming that the wave is planar and propagating along the great circle path, we combined different subgroups of OBSs to determine the apparent phase velocity along sections of the linear array (Fig. 1). The lowest velocities are found on a subarray straddling the ridge out to an age of about 0.8 million years ago (Ma) on either side, 55 to 60 km from the axis. Average apparent velocities across subarrays confined to sea floor older than 1.5 Ma exceed 3.8 km/s at a 25-s period, suggesting that the dominant effects of melting are present beneath sea floor less than about 2 Ma in age. There is also asymmetry between the eastern and western flanks of the ridge, with slower velocities beneath the western flank at periods less than 40 s. This asymmetry may reverse at periods greater than 40 s, but the statistical significance is questionable.

To improve the precision and search for anisotropy and along-axis variations in veloc-

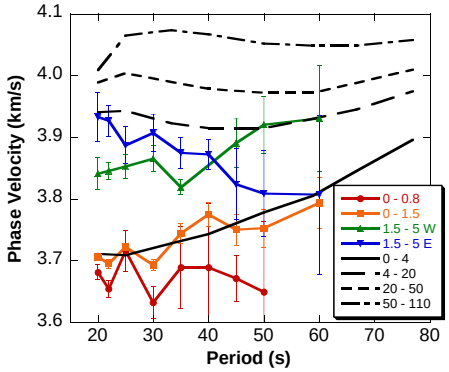

Fig. 1. Apparent phase velocities of Rayleigh waves for a single event along subsections of the primary OBS array (colored symbols) compared with previous teleseismic determinations of average velocities (black lines) as a function of age of the Pacific sea floor (*5*). Legend gives ages of sea floor in millions of years. "W" and "E" indicate west and east of the axis, respectively. Error bars indicate 1 SD. At periods of less than 40 s, note the large jump in velocities from sea floor less than 1.5 Ma in age to that greater than 1.5 Ma, indicating the presence of melt in the upper 100 km beneath very young sea floor.

D. W. Forsyth, Department of Geological Sciences, Brown University, Providence, RI 02912, USA.
S. C. Webb and L. M. Dorman, Scripps Institution of Oceanography, University of California San Diego, La Jolla, CA 92093, USA.
Y. Shen, Woods Hole Oceanographic Institution, Woods Hole, MA 02543, USA.

*To whom correspondence should be addressed at donald_forsyth@brown.edu

ity, we needed to include the data from all the events (Fig. 2) and to account for nonplanar wavefronts. In the corners of the study area, it was not possible to resolve the velocity, because the rays all have similar azimuths and it cannot be determined where anomalies are distributed along the path. Within the interior of the array, coverage was dense enough to resolve regions as small as 100 km by 100 km. Our data are insufficient for complete resolution of both azimuthal and spatial variations. We thus reduced the nonuniqueness by assuming that the A_1 and A_2 terms are a function only of distance east or west from the ridge axis, whereas the isotropic component A_0 is a function of both latitude and longitude (*9*). This means that we solved for a two-dimensional variation in isotropic phase velocity but limited the solution for anisotropy to one-dimensional variations parallel to spreading.

To account for nonplanar wavefields (*10*), we represented the incoming wavefield from each earthquake as the sum of two plane waves, each with initially unknown amplitude, phase, and propagation direction. Although this two–plane-wave assumption is an approximation to a more complex wavefront, it is successful in representing with a minimum number of parameters the relatively slow variations in amplitude observed across the array. The addition of wavefield parameters and the use of amplitude information (*11*) make the tomographic inversion nonlinear, so we iterated to a solution using a linearized approach with the wavefield parameters damped to prevent large changes in parameter values in any one step.

Two images of the lateral distributions of phase velocity and anisotropy at 25 s are presented here (Fig. 3) to demonstrate the robustness of the primary features and the variability that is possible with different inversion approaches (*12*). Both models began from a starting model that is isotropic and symmetric about the ridge axis, with the variation of velocity with distance from the axis optimized by a previous inversion. In model 1 (Fig. 3A), the image was formed by inverting for the smoothest change to the starting model, with anisotropy taken as a function of distance from the axis with no requirement of symmetry. The smoothing parameter is relatively strong. In model 2 (Fig. 3B), the image was formed with a minimum length criterion that corresponds to weaker damping than in model 1. In both models, the reduction in variance from a

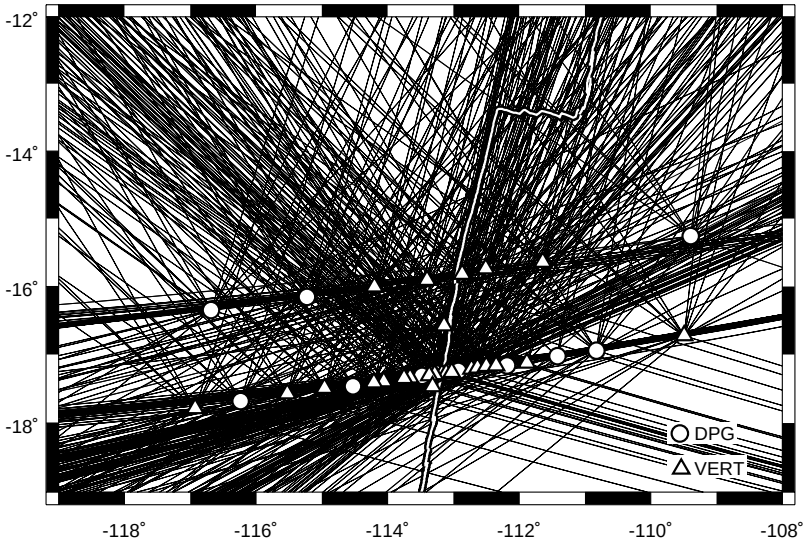

Fig. 2. Great circle paths from earthquakes to OBSs. At a 25-s period, 703 paths from 23 earthquakes to 39 stations (open symbols) were used in the tomographic inversion. Map area is the same as Fig. 1 of (*13*). The white line marks the spreading center. Open triangles show vertical component stations (VERT), and open circles show DPGs.

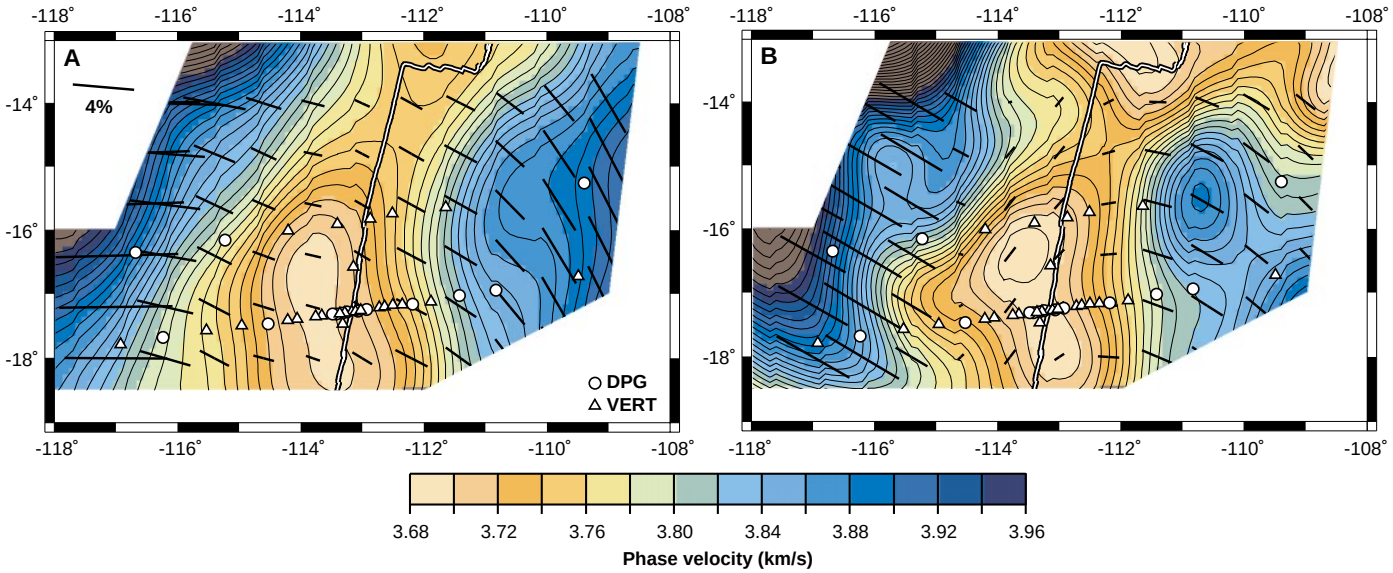

Fig. 3. Tomographic images of Rayleigh wave phase velocities at a period of 25 s. The region shown corresponds to the area with a good population of crossing rays. Resolution is poor at the edges, as can be seen by comparing the two models. Contours are at 0.01-km/s intervals; color changes are at 0.02-km/s intervals. Open triangles show vertical component stations, and open circles show DPGs. The white line marks the location of the plate boundary. Bars indicate direction and degree of azimuthal anisotropy. In these models, anisotropy varies only as a function of distance east or west of the ridge axis, but values are shown on a north-south grid to illustrate interpolated values between the nodes used in the inversion (*12*). (**A**) Inversion with a strong smoothing constraint; the starting model is a symmetric function of distance from axis. (**B**) Inversion with a weak minimum length constraint; the starting model is a symmetric function of distance from axis.

uniform velocity model is about 55%. The best-constrained region is between 117° and 110.5°W and within the array.

The dominant feature in all models is an increase in velocity away from the ridge axis. Minimum phase velocities at 25 s are 3.68 ± 0.02 km/s, within the range that requires melt to be present in the mantle. There is a broad region of low velocities; within the array, the area with velocities less than 3.80 km/s is more than 400 km wide, suggesting that upwelling and melting take place in a broad region. Dynamic flow apparently does not concentrate all the melting into a narrow column beneath this ridge axis, as had been suggested in some models of buoyant upwelling beneath the ridge (*13*).

Within the array, the lowest velocities are centered to the west of the axis. Typically, the minimum is reached 50 to 100 km to the west. In all models, the velocity in this region increases to the north of 16°S. In model 2 (Fig. 3B), there is a circular minimum centered at about 16.5°S, 113.7°W. Models begun with a uniform starting velocity, models with no anisotropy allowed, and models with weaker smoothing or minimum length constraints all have a circular low to the west of the axis that is more pronounced than is shown in either of these models. Only by imposing strong smoothing constraints and a symmetric, age-dependent starting model can the circular low be eliminated (Fig. 3A), but, even in this case, there is still a strong gradient to the north. There is a distinct change in overall orientation of the ridge axis at the overlapping spreading center (OSC) at 15°55′S that approximately coincides with the beginning of the gradient [Fig. 1 of (*13*)] and a cessation of recent off-axis volcanism (*14*), perhaps indicating a change in the pattern of mantle flow and melt production. It is possible that small-scale convection that may have been responsible for formation of the volcanic Sojourn Ridge [Fig. 1 of (*13*)] could disrupt the upwelling pattern beneath the ridge in this area.

The asymmetry in phase velocities across the axis is consistent with other observed asymmetries. Shear wave splitting is twice as large on the west side of the ridge as on the east (*15*). Shear wave delays across the axis are asymmetric, with later arrivals to the west (*16*). Sea floor on the Pacific side subsides more slowly, has lower mantle Bouguer anomalies, and is populated by more seamounts, all indicators of higher temperatures or greater off-axis melt production (*14*). There is an asymmetry in the shape of the axial high that could be caused by lower viscosities and higher temperatures to the west of the axis (*17*). Sea-floor spreading is asymmetric such that accretion is faster on the east (*14*), which makes the ridge migrate faster to the west in the direction that would keep the spreading center above the region of lower velocities and higher apparent melt concentration. In the Lau back arc basin, the slowest upper mantle velocities are also offset to the west of the spreading ridge (*18*), suggesting that such offsets may be a common feature of spreading centers.

The minimum in velocity at 16.5°S is intriguing because there is a $^3He/^4He$ isotopic anomaly observed in mid-ocean ridge basalt glasses centered at about 17°S on the EPR and other isotopic anomalies beginning at about 16°S extend southward to the OSC at about 21°S (*19*). It is not clear whether there is an upwelling center (*19*) or just an enriched, embedded heterogeneity within a mantle that has a southward component of motion (*20*), but in either case, enhanced melt production might be expected at this location. To the west of the axis at 16.5°S, there is a mantle Bouguer low [Fig. 2B in (*14*)], indicating either thicker crust or lower densities in the uppermost mantle. We suggest that there currently is a higher concentration of melt beneath the velocity low at 16.5°S generated by a compositional heterogeneity or upwelling that connects back to the ridge near 17°S and that this anomaly may be responsible for the robustness of the axial high and the propagation of OSCs away from 17°S (*21*). The northern boundary of the region affected by the melting anomaly is marked by the OSC at 15°55′S, which has not migrated.

Propagation of the Rayleigh waves is anisotropic. If uniform anisotropy is assumed for the entire region, the best solution gives a fast direction of N115°E and 1.8 ± 0.3% peak-to-peak anisotropy. This result is comparable to the average values inferred teleseismically for the eastern Pacific (*5*). Our models find a minimum in anisotropy centered on the ridge or somewhat to the west in the vicinity of the velocity minimum. The amplitude of the anisotropy increases to the west to about 3 to 5%. To the east of the axis, amplitudes are 2 to 3% and gradually rotate to a more southeasterly direction with distance from the axis.

The pattern of azimuthal anisotropy is consistent with predictions that there will be little azimuthal anisotropy where the crystallographic *a* axis of olivine is preferentially aligned vertically in upwelling flow and that anisotropy will increase with rotation to a more horizontal orientation aligned with plate motion as the flow diverges away from the spreading center (*22*). The broad region of low anisotropy found with the minimum length criterion (Fig. 3B) coincides with the broad region of low velocities. This correspondence could also be explained if the presence of melt enhances diffusion creep (*23*) to the point that it is the dominant deformation mechanism. Lattice-preferred orientation (LPO) of olivine crystals is generated through dislocation creep, but diffusion creep produces no substantial LPO (*24*).

Rayleigh waves at a 25-s period provide strong constraints on the lateral distribution of melt in the 20- to 70-km depth range. It is clear that melt is distributed over a broad region and is not confined to a narrow upwelling zone at the ridge axis. The amount of melt is not well constrained; it could vary from a few tenths of a percent if distributed in thin films to perhaps 5% if concentrated in tubes or pockets (*4*).

REFERENCES AND NOTES

1. To first order in an anisotropic medium, the sensitivity is equivalent to that of a vertically polarized *S* wave traveling horizontally.
2. R. S. White, D. McKenzie, R. K. O'Nions, *J. Geophys. Res.* **97**, 19683 (1992).
3. C. H. Langmuir, E. M. Klein, T. Plank, in *Mantle Flow and Melt Generation at Mid-Ocean Ridges,* J. Phipps Morgan, D. K. Blackman, J. Sinton, Eds. (American Geophysical Union, Washington, DC, 1992), pp. 183–280.
4. D. W. Forsyth, in *Mantle Flow and Melt Generation at Mid-Ocean Ridges,* J. Phipps Morgan, D. K. Blackman, J. Sinton, Eds. (American Geophysical Union, Washington, DC, 1992), pp. 1–65.
5. C. E. Nishimura and D. W. Forsyth, *Geophys. J. Int.* **96**, 203 (1989).
6. J.-P. Montagner and T. Tanimoto, *J. Geophys. Res.* **96**, 20337 (1991).
7. J.-P. Montagner and H. C. Nataf, *ibid.* **91**, 511 (1986).
8. Rayleigh waves have a dilatational or volumetric component that can be detected on differential pressure gauges (DPGs) in addition to the vertical and horizontal seismometers. We used vertical records whenever possible. An empirical transfer function was derived to convert pressure records into the equivalent vertical record. Transfer functions were also used to convert the responses of instruments from different OBS groups into the equivalent of a single type of vertical seismometer. The useful period range with good signal-to-noise ratios (minimum 3:1) and coherent arrivals from station to station is a function of earthquake magnitude, distance, and location, as well as instrument type and noise characteristics. The period range with the best coverage is 25 to 30 s.
9. Velocities in the medium are controlled by values of A_0, A_1, and A_2 at a grid of nodal points. The phase velocity at every point in the medium, including at the nodal points, is assumed to be a weighted average of values at neighboring nodal points. Weighting function is a Gaussian function of distance to the node, with characteristic falloff distance about equal to the wavelength of the wave.
10. Ray paths for surface waves deviate from great circle paths because of refraction by lateral heterogeneities. It is therefore customary in array analysis to solve for the azimuth and slowness of the best fitting plane wave. A more serious problem is multipathing or scattering or the effects of a complex wavefront, which produce interference between packets of energy of the same frequency arriving at a station along different paths. This interference causes characteristic amplitude variations across the array and phase shifts that can seriously distort apparent phase velocities measured with the assumption of planar waves (*25*). We found amplitude variations of a factor of three or more across the MELT array that were adequately modeled by two interfering plane waves. In one typical inversion, for the 23 events, the average, normalized amplitude and standard deviation were 0.68 ± 0.20 for the larger plane wave and

0.23 ± 0.30 for the smaller wave. Average departure from the great circle path was 1.8 ± 4.1° for the larger wave and −2.2 ± 9.4° for the smaller.
11. Because amplitudes carry information about the wavefield interference, at each frequency, we modeled the real and imaginary components for each record, rather than just the phase. Amplitudes are corrected for geometrical spreading on a uniform sphere, instrument-site response, and attenuation. In our tomographic inversions, we solved simultaneously for the velocity parameters and the six wavefield parameters per event. In an inversion that attempts to match all the amplitudes from all events simultaneously, we found the best attenuation factor for the region as a whole and the best, single amplitude correction factor for each station. At 25 s, the attenuation quality factor Q is ≥ 125.
12. In a nonlinear inversion, the results may depend on model assumptions. We ran more than 80 different inversions with different starting models, grids, and approaches to damping to understand which features of the models are robust. In the interior of the grid, we applied either a smoothness criterion so that the inversion will tend to find the smoothest set of changes to the starting model that satisfies the data or a damping criterion that tends to minimize the size of the changes to the starting model. In the inversions presented in Fig. 3, we used a 13 by 15 grid of velocity nodal points, spaced 1° apart from 11° to 20°S and extending 6° to the east and west of the ridge axis. Near the center of the grid and near the axis, points are spaced 0.5° apart. At each latitude, the grid points are shifted so that the center of the grid is at the ridge axis. The outer grid points are only lightly damped so that their values are free to vary to represent time delays that accumulate outside the area of interest.
13. The MELT Seismic Team, *Science* **280**, 1215 (1998).
14. D. S. Scheirer, D. W. Forsyth, M.-H. Cormier, K. C. Macdonald, *ibid.*, p. 1221.
15. C. J. Wolfe and S. C. Solomon, *ibid.*, p. 1230.
16. D. R. Toomey, W. S. D. Wilcock, S. C. Solomon, W. C. Hammond, J. A. Orcutt, *ibid.*, p. 1224.
17. M. A. Eberle and D. W. Forsyth, *Nature,* in press.
18. D. Zhao *et al.*, *Science* **278**, 254 (1997).
19. J. J. Mahoney *et al.*, *Earth Planet. Sci. Lett.* **121**, 173 (1994).
20. M. D. Kurz, J. J. Mahoney, J. M. Sinton, in preparation.
21. M.-H. Cormier, D. S. Scheirer, K. C. Macdonald, *Mar. Geophys. Res.* **18**, 53 (1996).
22. D. K. Blackman *et al.*, *Geophys. J. Int.* **127**, 415 (1996).
23. G. Hirth and D. L. Kohlstedt, *J. Geophys. Res.* **100**, 1981 (1995).
24. S. Karato and P. Wu, *Science* **260**, 771 (1993).
25. W. Friederich, E. Wielandt, S. Stange, *Geophys. J. Int.* **119**, 931 (1994).
26. P. Wessel and W. H. F. Smith, *Eos* **72**, 441 (1991).
27. This project is part of the Ridge Inter-Disciplinary Global Experiments program and is funded by the NSF. We thank D. Scheirer and S.-H. Hung for help in generating maps and handling data and C. Wolfe for a constructive review. The Generic Mappings Tools plotting program (*26*) was used in several figures.

18 February 1998; accepted 21 April 1998

The Radio-Frequency Single-Electron Transistor (RF-SET): A Fast and Ultrasensitive Electrometer

R. J. Schoelkopf,* P. Wahlgren, A. A. Kozhevnikov, P. Delsing, D. E. Prober

A new type of electrometer is described that uses a single-electron transistor (SET) and that allows large operating speeds and extremely high charge sensitivity. The SET readout was accomplished by measuring the damping of a 1.7-gigahertz resonant circuit in which the device is embedded, and in some ways is the electrostatic "dual" of the well-known radio-frequency superconducting quantum interference device. The device is more than two orders of magnitude faster than previous single-electron devices, with a constant gain from dc to greater than 100 megahertz. For a still-unoptimized device, a charge sensitivity of $1.2 \times 10^{-5}\ e/\sqrt{\text{hertz}}$ was obtained at a frequency of 1.1 megahertz, which is about an order of magnitude better than a typical, 1/*f*-noise-limited SET, and corresponds to an energy sensitivity (in joules per hertz) of about 41 $\hbar$.

Methods for performing more-sensitive electrical measurements are often instrumental in enabling new physics and technology. Improvements in measurements can be accomplished either through refinement of traditional devices or by developing devices that rely on different physical principles. An example of the latter are superconducting quantum interference devices (SQUIDs), which use the phenomenon of flux quantization in a superconducting loop and are the most sensitive magnetometers (*1*) available. Besides magnetometry, SQUIDs have also been adapted to a wide range of applications where amplifiers are needed for low-level signals and low-impedance sources.

We report the development of an extremely sensitive electrometer, based on a new type of SET—the radio-frequency SET or RF-SET. First proposed by Averin and Likharev (*2*) and demonstrated by Fulton and Dolan (*3*), the SET is the electrostatic "dual" (*4*) of the SQUID and is able to measure a small fraction of an electron's charge. As such, single-electron devices are complementary to SQUIDs and should be the measurement technology of choice for sensitive, high-impedance applications. However, conventional SET-based electrometers have been limited by slow operation speeds, typically 1 kHz or less. Furthermore, the charge sensitivity at these low frequencies, while typically much higher than that of conventional electrometers, is limited by 1/*f* noise (*5*) due to the motion of background charges. The RF-SET, however, can operate even at frequencies in excess of 100 MHz, where the 1/*f* noise due to background charge motion is completely negligible. In fact, we describe how optimized versions of this device could allow electrometry at the quantum limit, with an energy sensitivity of a few $\hbar$ ($\hbar \equiv 1.054 \times 10^{-34}$ J/Hz).

With the advent of this truly high-speed and more sensitive electrometer, many of the proposed applications of single electronics, including an electron-counting current standard (*6*) and advanced photodetectors (*7*), become much more practical. For example, at the present performance levels, the RF-SET has the sensitivity and speed to count electrons at frequencies >10 MHz (that is, measure a current on the order of picoamperes, electron by electron) with very good signal-to-noise (S/N) ratio. New physics experiments can be envisioned in "single-charge dynamics," such as the direct observation of Bloch and single-electron tunneling oscillations (*2, 8*), and the monitoring of tranport processes at the single-charge level in a variety of systems.

Most Coulomb blockade (SET) electrometers use a double-junction structure with a central metallic island that is capacitively coupled to the input. Under the proper conditions, such a device has an onset of current that is controlled by the potential of the island. The onset is periodic in the gate charge, q_g, coupled onto the island via the gate capacitor, with a period equal to the charge of a single electron, e. The gate charge, q_g, can be continuously varied and is defined as $q_g = C_g V_g$, where C_g is the gate capacitance and V_g is the gate voltage. Usually, the SET is current-biased just above threshold, and the drain-to-source voltage is monitored with a high-impedance voltage amplifier at room temperature. Despite their limitations, such SET electrometers have already been used to observe macroscopic charge quantization (*9*), to characterize the performance of single-electron pumps and traps (*10, 11*), and to measure the local chemical potential variations (*12, 13*) of semiconducting systems.

In order to display a strong Coulomb blockade and the desired sharp onset of

R. J. Schoelkopf, A. A. Kozhevnikov, D. E. Prober, Departments of Applied Physics and Physics, Yale University, New Haven, CT 06520–8284, USA.
P. Wahlgren and P. Delsing, Department of Microelectronics and Nanoscience, Chalmers University of Technology and Göteborg University, S-412 96 Göteborg, Sweden.
*To whom correspondence should be addressed. E-mail: rob.schoelkopf@yale.edu